

# Receiver functions from regional $P$ waves

Jeffrey Park and Vadim Levin

Department of Geology and Geophysics, Yale University, New Haven, CT 06520, USA. E-mails: park@geology.yale.edu; vadim@geology.yale.edu

Accepted 2001 April 17. Received 2001 January 29; in original form 2000 June 23

## SUMMARY

$P$  waves from regional-distance earthquakes are complex and reverberatory, as would be expected from a combination of head waves, post-critical crustal reflections and shallow-incident  $P$  waves from the upper mantle. Although designed for steeply-incident teleseismic  $P$  waves, receiver functions (RFs) can also retrieve information about crustal structure from regional  $P$ . Using a new computation method based on multiple-taper spectral analysis, regional-distance RFs for GSN stations RAYN and ANTO show broad agreement with teleseismic RFs. At RAYN the moveout of the Moho-converted  $P_s$  phase, relative to direct  $P$ , follows the predictions of the IASP91 earth model well. The Moho-converted  $P_s$  phase shows complexity associated with the transition-zone triplications near  $\Delta=20^\circ$  and constant delay (zero moveout) as  $\Delta\rightarrow 0$ , consistent with conversion from  $P_n$ . Similar behaviour is seen for ANTO for events that arrive from the west. For eastern backazimuths the ANTO RFs show features whose moveout is negative as  $\Delta\rightarrow 0$ . This moveout is poorly fit by reverberations in flat layers or by direct scattering from a dipping interface, but is consistent with a topographic scatterer 20–30 km eastward of the ANTO site. Regional receiver functions may therefore be useful in judging whether teleseismic RFs at a particular station are suitable candidates for a 1-D velocity structure inversion. Synthetic seismograms of regional  $P$  phases, computed with a locked-mode reflectivity approach in a 1-D structure, confirm several gross features of the RAYN and ANTO regional receiver functions.

**Key words:** anisotropy, body waves, crustal structure, Moho discontinuity, seismic coda, synthetic seismograms.

## 1 INTRODUCTION

Seismic signals from earthquakes at regional distances (200–1000 km) are complex, containing considerable scattered energy. Raytrace models in simple crust-mantle structures suggest that the initial  $P$  phases can contain true head waves that propagate along the Moho, whispering-gallery phases that refract in the uppermost mantle, and crustal reverberations.  $P$ -to- $S$  scattering is evident in the development of a high frequency coda within the initial  $P$  arrivals (e.g. Dainty & Toksoz 1990; Menke *et al.* 1990; Wagner & Langston 1992a). For teleseismic  $P$  waves, receiver-function (RF) analysis (Burdick & Langston 1977; Langston 1981) estimates  $P_s$  converted energy from buried interfaces in the shallow Earth. RF analysis uses vertical seismic motion to predict motion in the radial and transverse horizontal directions, to estimate  $P$ - $SV$  and  $P$ - $SH$  scattering, respectively. Theoretically, this principle should apply to shallow-incident  $P$  waves and  $P$  waves trapped in the crustal waveguide. If so, estimates of Moho depth and the depths of major crustal interfaces, usually the target of wide-angle active-source refraction surveys, could be made from the regional body phases of small earthquakes.

Popular methods for estimating RFs involve either damped spectral division (Ammon 1991) or time-domain deconvolution (Gurrola *et al.* 1995), but are subject to instability from various scattering sources e.g. shallow resonances and multiply-scattered waves. RF stacking (Sandvol *et al.* 1998a,b) or simultaneous inversion of multiple seismic records (Abers *et al.* 1995) at a given station can reduce spurious features, but receiver function analysis has mostly been restricted to frequencies  $f < 1$  Hz, and often to  $f \lesssim 0.2$  Hz. A new RF-estimation method based on multiple-taper spectral correlation (Park & Levin 2000) appears to resist instability in the face of scattering, and offers a new method for multiple-record RF estimation. Using multiple records, estimates of  $P$ -to- $S$  conversions at frequencies approaching 5 Hz can be obtained with the spectral correlation method. The  $P_s$  converted phases can be retrieved consistently from earthquakes at varying epicentral distances, from both mantle  $P$  and core-refracted  $PKP$  phases.

This paper examines the feasibility of using this method of RF analysis on regional  $P$  waves to investigate buried interfaces in the crust and uppermost mantle. We show results from two permanent broadband observatories of the Global Seismographic Network (GSN) in the Middle East region:

RAYN (Ar Rayn, Saudi Arabia) and ANTO (Ankara, Turkey). RAYN lies atop the stable Arabian shield, while ANTO lies within the actively deforming Anatolian peninsula. The two distinct crustal environments lead to distinct reverberation patterns in receiver functions estimated from both teleseismic and regional-distance earthquakes.

## 2 DATA AND TECHNIQUE DESCRIPTION

We chose two seismic stations in the Middle East, RAYN (Ar Rayn, Saudi Arabia) and ANTO (Ankara, Turkey), that have abundant seismicity within ‘regional’ distances (up to 1000 km). For both stations, we retrieved earthquake data for events located at all distances. To facilitate a search for shared features, we selected distant and regional earthquakes that lay within similar backazimuthal ranges. RAYN is on an exposed Proterozoic shield, near the edge of the thick sediments of the Arabian platform. Seismicity within Arabia is scarce, but the Zagros active convergence zone of southern Iran lies at regional distances in the backazimuthal range  $30^{\circ}$ – $80^{\circ}$  (Fig. 1). We analyzed 128 regional events for RAYN, with  $M \geq 4.5$ . 35 teleseismic events with  $M \geq 6.3$  were chosen for analysis in backazimuthal range  $45^{\circ}$ – $115^{\circ}$ , corresponding to the southern Asian convergence zones and the subduction zones of the southwest Pacific. ANTO lies in a region of active tectonism, as Anatolia undergoes westward translation to ‘escape’ the collision of the Arabian and Eurasian plates (Kahle *et al.* 1999; Gok *et al.* 2000). Therefore significant events at all regional distances are available. We analysed 130 regional and teleseismic waves at ANTO for events within the backazimuthal range  $70^{\circ}$ – $130^{\circ}$  (Fig. 2), using a  $M = 5.0$  regional cutoff and a  $M = 6$  teleseismic cutoff. We separately analysed 53 regional events at western back-azimuths, from western Turkey and the Aegean Sea.

In receiver-function analysis, the vertical-component record of a  $P$ -coda, assumed to contain mostly  $P$ -wave motion, is used to predict the records of radial- and transverse-horizontal seismic motion. The direct  $P$  wave and all  $P$ -reverberations with

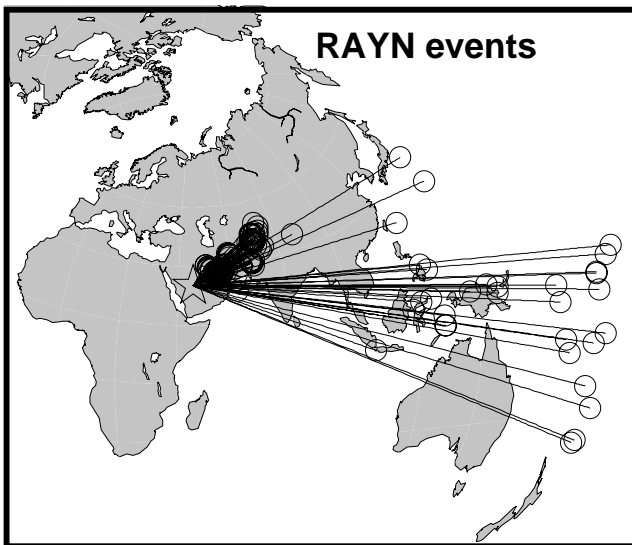


**Figure 1.** Regional and teleseismic events at eastern backazimuths relative to RAYN, used to estimate receiver functions. Events from 1996–1998 are included. The map is a rectangular mask of an azimuthal equidistant projection, centred on RAYN.

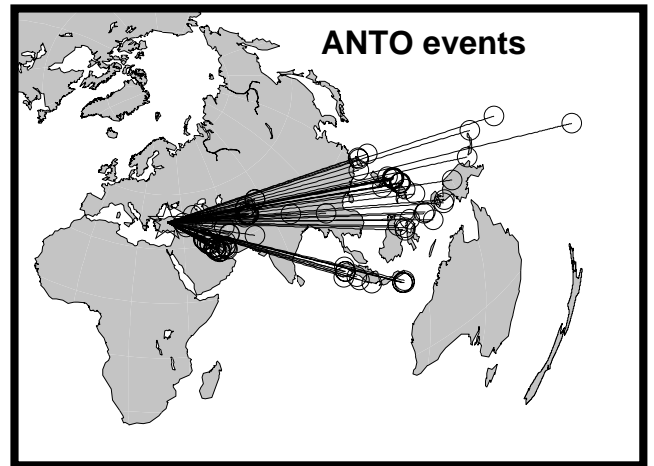


**Figure 2.** Regional and teleseismic events at eastern backazimuths relative to ANTO, used to estimate receiver functions. Events from 1993–1997 are included. The map is a rectangular mask of an azimuthal equidistant projection, centred on ANTO.

direct- $P$  phase velocity appear on the horizontal components as a scaled version of the vertical component. Other motion on the horizontal components, which may include  $P_s$  converted phases, side-scattered  $P$  or local resonances, is generated by the interaction of direct  $P$  with the structure beneath and around the seismometer. In principle the scattering can be deconvolved from the  $P$  coda as a series of pulses at finite delay relative to direct  $P$ , in effect, modelling the horizontal-component motion as a linear combination of time-lagged copies of the vertical-component motion. Spectral division is the simplest way to estimate a receiver function:  $H_R(f) = Y_R(f)/Y_Z(f)$  and  $H_T(f) = Y_T(f)/Y_Z(f)$ . Here  $Y_Z(f)$ ,  $Y_R(f)$ , and  $Y_T(f)$  are the Fourier spectra of the vertical, radial and transverse seismic components, respectively. The spectral-domain receiver functions  $H_R(f)$  and  $H_T(f)$  can be transformed into a prediction filter of  $P_s$  scattered waves by performing the inverse Fourier transform on them.

We estimated receiver functions using the multiple-taper spectral correlation technique (Park & Levin 2000), a variant of damped spectral division (Ammon 1991). The multitaper algorithm has two advantages. First, it estimates the spectral ratios  $H_R(f) = Y_R(f)/Y_Z(f)$  and  $H_T(f) = Y_T(f)/Y_Z(f)$  only from the portion of the horizontal motion that is correlated (in a narrow frequency band) with the vertical motion. Second, the proportion of correlated horizontal motion, quantified by the spectral coherence  $C(f)$ , is used to estimate the uncertainty of  $H_R(f)$  and  $H_T(f)$ . These uncertainties can be used to handicap RF estimates from different earthquakes when estimating a composite, or ‘stacked,’ receiver function. In the composite sum we handicap single-record RF estimates by their uncertainties, so that greater weighting is given to high-coherence RF estimates. All stacking is performed in the frequency domain. There is no formal uncertainty estimate for the time-domain multitaper RF, but an informal assessment can be made from the acausal part of the RF i.e. the amplitude of  $H_R(t)$ ,  $H_T(t)$  for  $t < 0$ . In our experience with real data, the coherence between horizontal and vertical motion in a  $P$  coda is frequency-dependent, and can vary greatly from event to event. Therefore the use of uncertainty-based weights in a multiple-record RF estimate is important.

We illustrate multitaper RF estimation with a regional  $P$  phase recorded at RAYN from an 11 January 1998 Zagros earthquake with  $m_b=4.7$  and  $\Delta=8.3^\circ$  (Fig. 3). Fig. 4 shows spectrum and spectral coherence estimates for the  $P$  coda, computed for 40-second data windows (800 point time-series) using

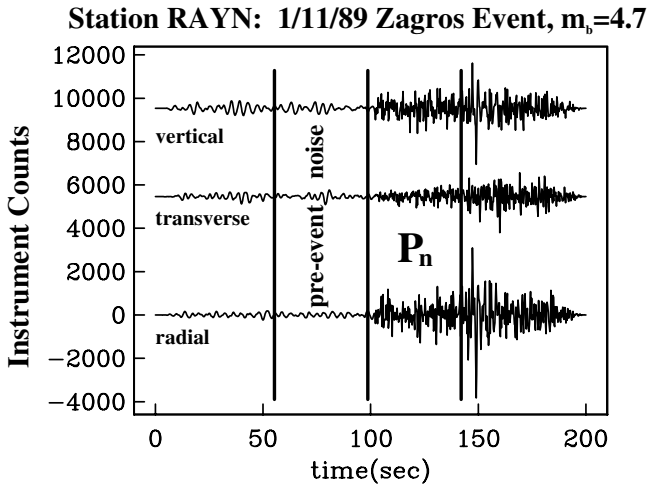


**Figure 3.** Example of regional  $P$  observed at RAYN (Ar Rayn, Saudi Arabia) from a modest earthquake ( $M_b=4.7$ ) in the Zagros mountains. Succeeding figures illustrate how the multiple-taper correlation algorithm estimates a receiver function from this data.

three Slepian tapers (Thomson 1982; Park *et al.* 1987; Lees & Park 1995) with time-bandwidth product  $p=2.5$  and upper cutoff frequency  $f_c=3.0$  Hz. Note that the  $P$ -wave spectrum on all components exceeds the spectrum of pre-event motion by an order of magnitude or more for  $f>0.5$  Hz, even for low-amplitude portions of the spectrum. However, signal and pre-event noise are comparable in the microseism passband. Note the large variations in coherence between horizontal and vertical components. Since the pre-event noise is small, the ‘noise’ relevant to RF analysis is primarily signal-generated.

Fig. 5 shows RF estimates in both frequency and time domains. We apply a cosine taper  $\cos^2(\pi f/2f_c)$  in the frequency domain to  $H_R(f)$ ,  $H_T(f)$  before the inverse Fourier transform to avoid spurious sharp-bandpass ringing in the time-domain RFs  $H_R(t)$ ,  $H_T(t)$ . The shallow incidence of the regional  $P$  phase leads to the large value of  $H_R(t)$  at  $t=0$ . Relative uncertainties in the transverse RF are larger than those in the radial RF, and lead to a larger acausal portion of the transverse receiver function in the time-domain. The acausal portion of the RF tends to decrease as  $H_R(f)$ ,  $H_T(f)$  from multiple events are combined to form a composite RF. Note that significant amplitude in  $H_R(t)$ ,  $H_T(t)$  is concentrated within 10 s of zero lag ( $t=0$ ). This concentration is in part dictated by the estimation algorithm, which averages spectral information over  $\Delta f=2pf_R=5f_R$ , where  $f_R=1/T$  is the Rayleigh frequency of a time series of length  $T$ . For a 40 s data series,  $\Delta f=(5/40)$  Hz = 0.125 Hz. With these parameters, the spectral averaging impedes

### Station RAYN: 1/11/98 Zagros Event, $m_b=4.7$

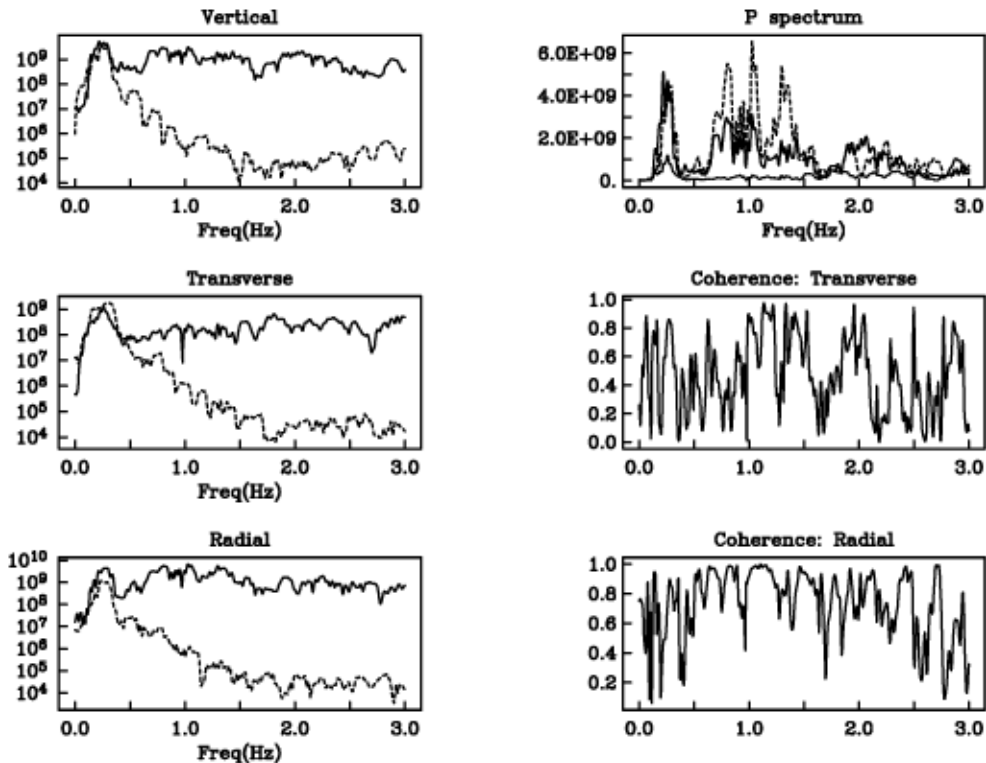


**Figure 4.** First step in multiple-taper correlation (MTC) receiver function estimation, applied to the  $P$  wave shown in Fig. 3. Log-linear plots in the left column plot the  $P$ -coda spectra (solid) versus pre-event noise spectra (dashed) for the three particle-motion components. Note that the signal-to-noise ratio is weak at low frequency where the teleseism background is large, but is quite large for  $f>1$  Hz. In the top-right panel the  $P$ -coda spectrum estimates of the vertical (solid), radial (coarse dash) and transverse (fine dash) components are superimposed. Also in the right column are plotted the squared coherence  $C^2(f)$  of the transverse and radial components, respectively, with the vertical component.

## Station RAYN: 1/11/98 Zagros Event, $m_b = 4.7$

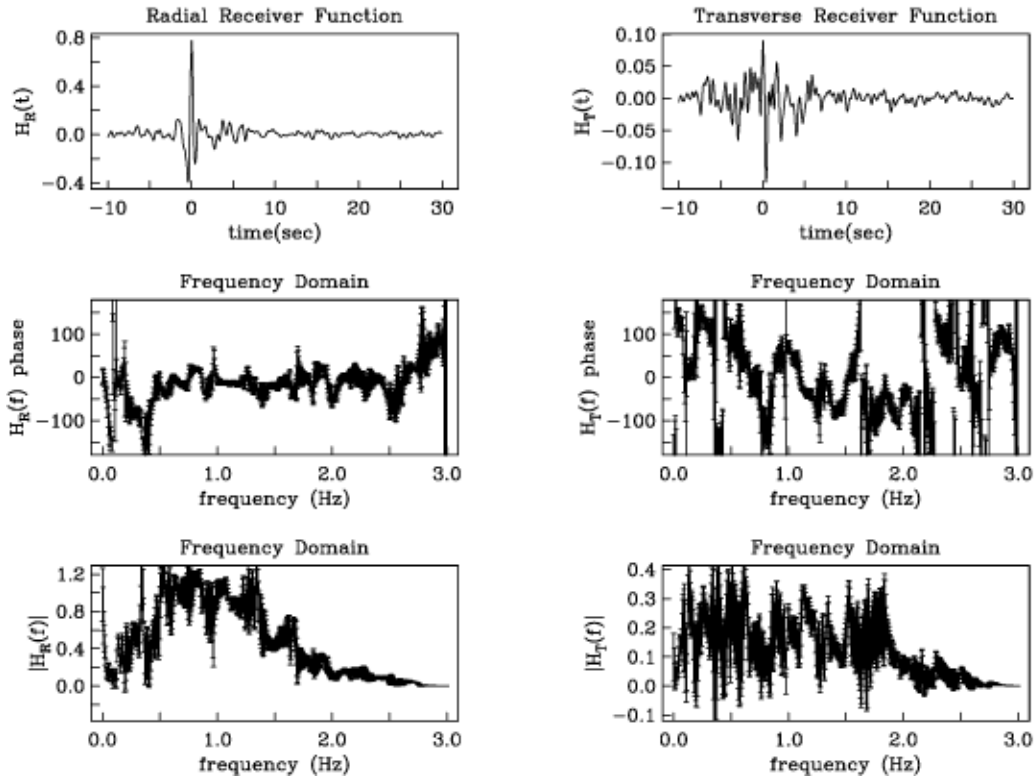


**Figure 5.** Second step in multiple-taper correlation (MTC) receiver function estimation, applied to the regional  $P$  wave shown in Fig. 3. The left column graphs the radial RF. The right column graphs the transverse RF. The top row graphs the RFs in the time-domain. The centre and bottom rows graph the phase and amplitude, respectively, of the complex-valued RF in the frequency domain, with error bars.

the recovery of time-domain features at time lags much larger than  $t = 1/(0.125 \text{ Hz}) = 8 \text{ s}$ . In order to retrieve longer prediction filters  $H_R(t)$ ,  $H_T(t)$ , one needs either a longer data record  $T$  or else a smaller time-bandwidth product  $p$ . The uncertainty of  $H_R(f)$ ,  $H_T(f)$  increases as the implicit spectral average narrows (scaled by  $p$ ), analogous to the resolution-versus-variance tradeoff in Backus–Gilbert inverse theory.

### 3 DATA ANALYSIS

#### 3.1 Arabian shield

We estimated receiver functions at RAYN as a function of epicentral distance  $\Delta$  (Figs 6 and 7), averaging data from sources in overlapping distance intervals. Data overlap causes adjacent traces in the RF profiles to be correlated. Features in the RFs that span three or more adjacent traces are not processing artifacts. Receiver functions from teleseismic sources display a number of features familiar from previous studies at RAYN (Sandvol *et al.* 1998b; Al-Amri 1999; Levin & Park, 2000). The conversion from the Moho (hereafter  $P_{MS}$ ) is a positive one-sided pulse on both the radial and the transverse components, at  $t \approx 4.75 \text{ s}$  for teleseismic events (Fig. 6). Preceding  $P_{MS}$  is a group of pulses at 2–3 s which also have positive polarity on the radial component, and much transverse energy. These phases are likely to be associated with a midcrustal interface (or interfaces), imaged by an active-source profile (Mooney *et al.* 1985; Prodehl 1985; Badri 1991) and also suggested by RF analysis (Levin & Park 2000).

Behind  $P_{MS}$  on the transverse component lies another positive polarity arrival,  $P_{HS}$ , that Levin & Park (2000) associated with the Hales discontinuity (Hales 1969; Hales *et al.* 1975). On the transverse RF, the polarity of  $P_{MS}$  and  $P_{HS}$  depends on back-azimuth, positive for arrivals from the east, negative for arrivals from the west. This polarity flip could be caused by an interface that dips either to the north or to the south, but would be inconsistent with the general north–south trend of terrane sutures within the Arabian Shield. Detailed modelling supports an alternative model, in which thin anisotropic layers with dipping axes of symmetry explain the shapes of  $P_{MS}$  and  $P_{HS}$  and their polarity switches (Levin & Park 2000). The  $P_{HS}$  phase appears only weakly on the radial component, though in limited distance ranges it is preceded by a different pulse ( $60^\circ$ – $90^\circ$  on the radial RF,  $120^\circ$ – $150^\circ$  on transverse RF).

Comparing receiver function features from ‘traditional’ distances ( $60^\circ$ – $90^\circ$ ) to those computed for the near-teleseismic and regional events (Figs 6 and 7), we identify  $P_{MS}$  readily for all epicentral distances on the radial RF, but less confidently on the transverse RF. A positive-polarity pulse prior to  $P_{HS}$  appears clearly in regional radial RFs at 7.5–8 s delay. The  $P_s$  delay estimate (corrected for phase velocity) suggests that the pulse has no clear counterpart in the far-teleseismic ( $\Delta > 60^\circ$ ) RFs. It may correspond to the initial part of a broad, weak positive feature seen at distances  $60^\circ$ – $80^\circ$ .

All  $P_s$  phases suggested by the RAYN RFs experience some temporal moveout as the epicentral distance decreases. The nature of the moveout is often consistent with that expected for an upgoing  $P_s$  converted wave. Close inspection of the radial

## Station RAYN: 3Hz cutoff

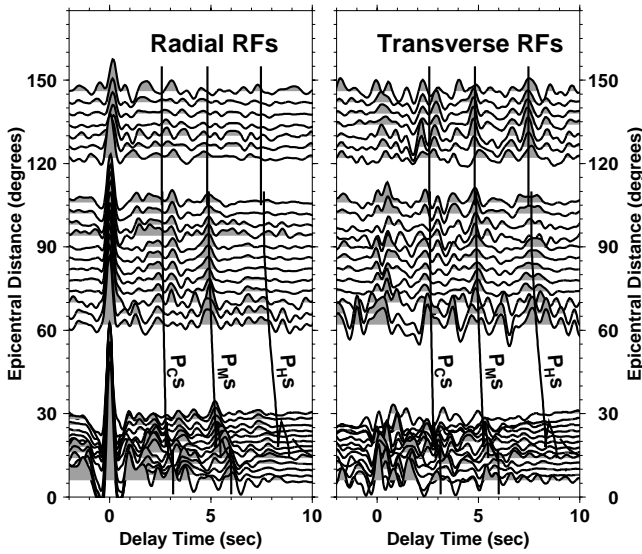


**Figure 6.** RAYN receiver functions, bin-averaged in the frequency domain, with uncertainty handicaps, in overlapping  $8^\circ$  and  $4^\circ$  epicentral-distance intervals. RFs for broadband data (20 sps) are shown for eastern backazimuths, with frequency cutoff  $f=3$  Hz. The transverse RFs are boosted in amplitude by a factor of two to facilitate visual comparison. Superimposed delay curves are computed for the three  $P_s$  converted phases (denoted  $P_{CS}$ ,  $P_{MS}$  and  $P_{HS}$ ) that would arise from interfaces at 21, 41 and 72 km depth in a simple velocity structure based on the model for RAYN suggested by Levin & Park (2000)—see Table 1. The phase velocities of incoming  $P$  and  $P_n$  waves are computed for a source at 15 km depth using the IASPEI91 model and software. The hypothetical head-wave conversion  $P_{ns}$  has a near-constant delay  $\sim 6$  s for  $0 < \Delta < 17^\circ$ .

RF in Fig. 7 suggests that in the range  $12^\circ < \Delta < 20^\circ$  the  $P_{MS}$  pulse bifurcates. An earlier pulse is evident at  $\sim 5$  s at all distances. It is relatively weak and positive on the radial RFs, and sharp and negative on the transverse RFs. A second pulse at 5.5–6.0 s is strong and positive on the radial RFs, and weak and positive on the transverse RF. The timing of the second pulse is appropriate for a  $P$ -to- $S$  conversion from a  $P_n$  phase, propagating horizontally at the Moho.

We analysed the same regional events at RAYN using data from the short-period channels, sampled at 40 samples per second (sps), leading to RF gathers with an effective corner frequency of 5–7 Hz (Fig. 8). Multiple  $P_s$  pulses at high-frequency appear to ‘move out’ with  $\Delta$  on the radial component—note the complexity for  $14^\circ < \Delta < 24^\circ$ . The transverse RFs are significantly less coherent with epicentral distance at these frequencies. In this epicentral range the  $P$  wave undergoes triplications in

**Table 1.** Isotropic velocity and density values for RAYN model, consistent with radial receiver functions. Values in the first column define lower boundaries of model layers.

Depth, km	$V_p$ , km s $^{-1}$	$V_s$ , km s $^{-1}$	$\rho$ , g cm $^{-3}$
1.2	5.0	2.85	2.2
21	6.3	3.7	2.7
41	7.0	4.0	2.9
72	8.15	4.7	3.1
$\infty$	8.3	4.8	3.3

## Station RAYN: 3Hz cutoff

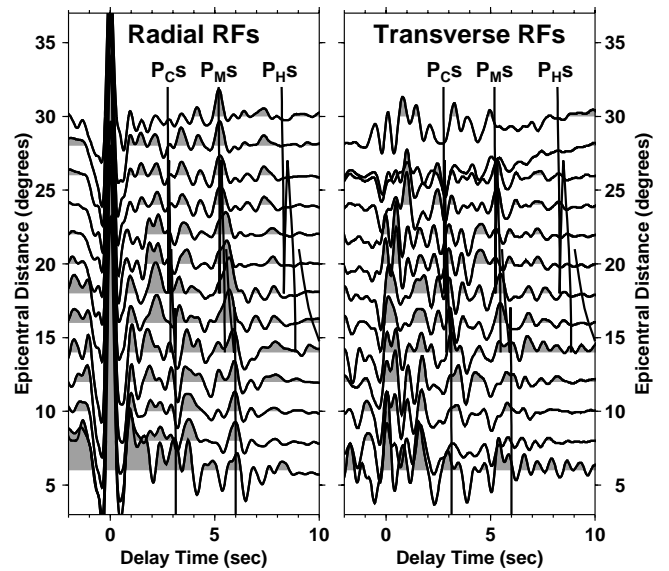


**Figure 7.** Regional and near-telesismic RAYN receiver functions, averaged in  $4^\circ$  epicentral-distance bins in the frequency domains with uncertainty handicaps. Results for broadband data (20 sps) are shown for eastern backazimuths, with frequency cutoff  $f=3$  Hz. Superimposed delay curves are computed for the three  $P_s$  converted phases (denoted  $P_{CS}$ ,  $P_{MS}$  and  $P_{HS}$ ) that would arise from interfaces at 21, 41 and 72 km depth in a simple velocity structure based on the model for RAYN suggested by Levin & Park (2000)—see Table 1. The phase velocities of incoming  $P$  and  $P_n$  waves are computed for a source at 15 km depth using the IASPEI91 model and software. The hypothetical head-wave conversion  $P_{ns}$  has a near-constant delay  $\sim 6$  s for  $0 < \Delta < 17^\circ$ .

traveltime, caused by velocity gradients in the mantle transition zone. Direct  $P$  in the triplication range is a composite of distinct phase velocities and incidence angles. It therefore leads to distinct  $P_s$  delays, consistent with the observed broadening of the  $P_{MS}$  pulse in the RAYN radial RFs.

## 3.2 Anatolia

Although data from RAYN suggests that regional-distance receiver functions can illuminate the crust–mantle transition, data from ANTO shows that this potential will not be realized in all cases. For ANTO the regional RFs are retrievable, and, for earthquakes at western backazimuths, Moho-converted  $P_s$  energy is evident at 5–6 s delay (Fig. 9), with moveout similar to the Moho  $P_s$  energy at RAYN. However, for eastern back-azimuths, shallow reverberations at frequencies  $f > 1$  Hz obscure primary  $P_s$  conversions from deeper interfaces. The raw amplitudes of the ANTO transverse RFs from the east (Fig. 10) are comparable to the radial RF amplitudes, an indicator of unusually large scattering. Direct  $P_s$  conversions from flat interfaces should have a positive moveout as  $\Delta$  decreases from teleseismic to regional values. The negative pulse on the radial RF that aligns at  $\sim 7$  s delay with the predicted  $P_s$  conversion from the Hales may be consistent with positive moveout, but little else seems to be. Many features are continuous in the RFs for  $\Delta$  from regional to teleseismic, but exhibit negative moveout as  $\Delta \rightarrow 0$ . With a 6 Hz frequency cutoff and narrower epicentral binning (Fig. 11) the continuity of features for  $\Delta < 35^\circ$  is less pervasive, but negative moveout as  $\Delta \rightarrow 0$  is still discernable.

**Station RAYN: 10Hz cutoff**

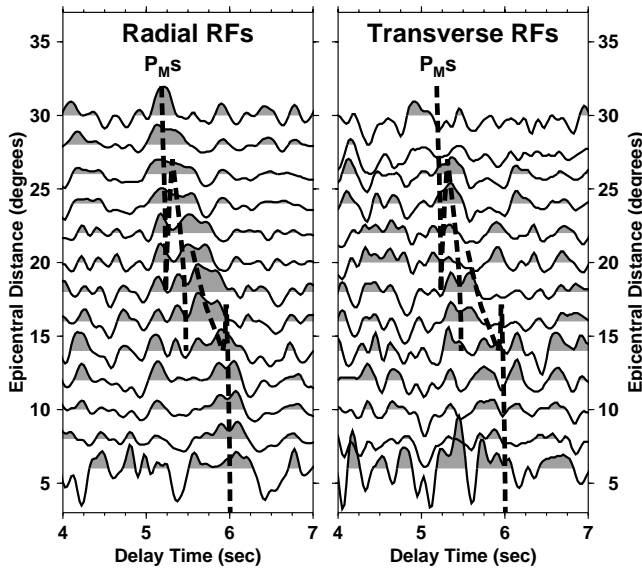


**Figure 8.** Regional and near-telesismic RAYN receiver functions, averaged in  $4^\circ$  epicentral-distance bins in the frequency domain with uncertainty handicaps. Results for short-period data (40 sps) are shown for eastern backazimuths, with frequency cutoff  $f=10$  Hz. Superimposed delay curves are computed for the  $P_{MS}$  converted phase that would arise from the Moho at 41 km depth in a simple velocity structure based on the model for RAYN suggested by Levin & Park (2000).

**Station ANTO: 3Hz cutoff**

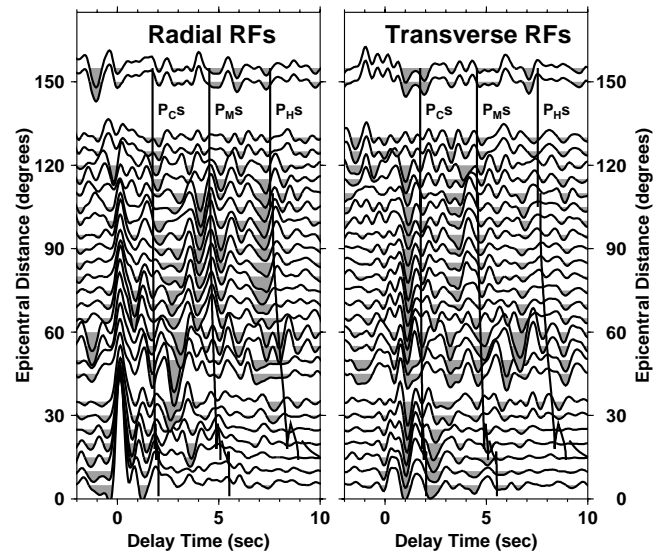


**Figure 10.** ANTO receiver functions, averaged in  $10^\circ$  epicentral-distance bins in the frequency domains with uncertainty handicaps. Results for events from eastern backazimuths are shown. The thin solid lines indicate predicted  $P_s$  arrival delays computed from the RAYN crustal model, denoted  $P_{CS}$ ,  $P_{MS}$  and  $P_{HS}$ , respectively, from a midcrustal interface, the Moho and a hypothetical Hales discontinuity. The RF traces are shaded on the negative side to highlight features whose delays decrease as  $\Delta \rightarrow 0$ , inconsistent with the moveout predicted for direct upgoing  $P_s$  phases. Continuity of RF pulses from telesismic to regional distances is evident at short delay times, but epicentral moveout appears opposite to that predicted for  $P_s$ .

**Station ANTO: 6Hz cutoff**

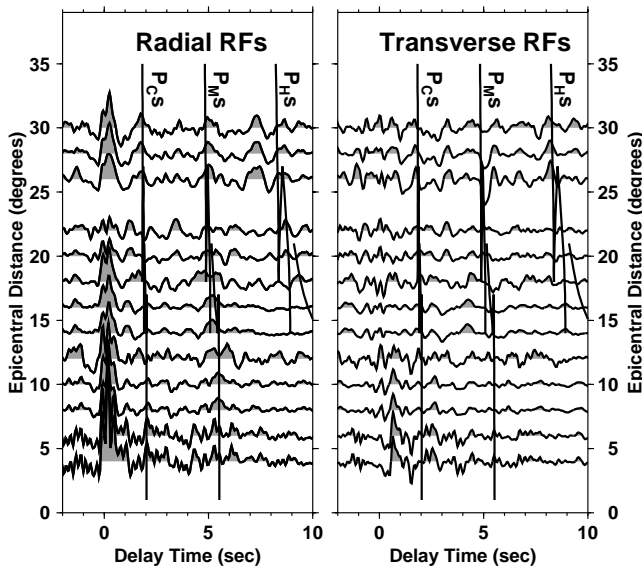


**Figure 9.** Regional receiver functions for station ANTO (Ankara, Turkey) from 53 events at western back-azimuths. The RF traces are averaged with uncertainty handicaps in the frequency domain using overlapping  $4^\circ$  bins. Two thin solid lines indicate predicted  $P_s$  arrival delays computed from the Sandvol *et. al.* (1998a) crustal model, denoted  $P_{CS}$ ,  $P_{MS}$ , respectively, from midcrustal and Moho interfaces. Another solid line indicates the delay time of a hypothetical  $P_{HS}$  converted phase from the Hales discontinuity. Note the concentration of pulse energy at 5–6 s delay, appropriate for a Moho-converted  $P_{MS}$ .

**Station ANTO: 6Hz cutoff**

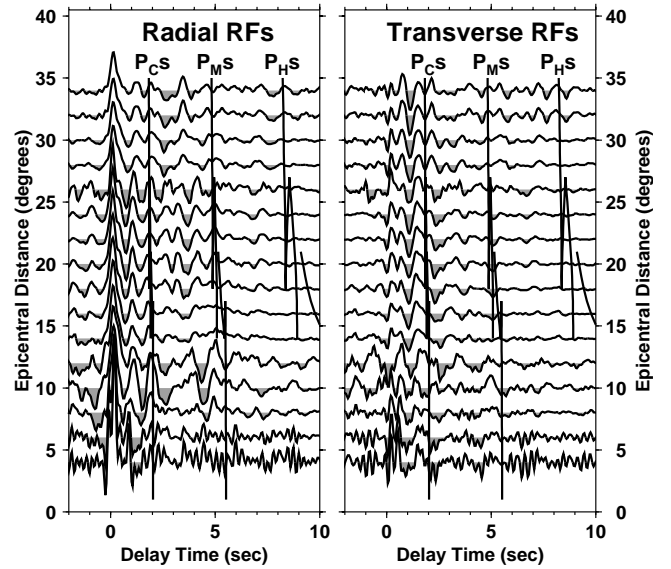


**Figure 11.** ANTO receiver functions, averaged in  $4^\circ$  epicentral-distance bins in the frequency domains with uncertainty handicaps. Results for events from eastern backazimuths are shown. The thin solid lines indicate predicted  $P_s$  arrival delays computed from the RAYN crustal model, denoted  $P_{CS}$ ,  $P_{MS}$  and  $P_{HS}$ , respectively, from a midcrustal interface, the Moho and a hypothetical Hales discontinuity. The RF traces are shaded on the negative side to highlight features whose delays decrease as  $\Delta \rightarrow 0$ , inconsistent with the moveout predicted for direct upgoing  $P_s$  phases.

To explain the negative  $P_s$  moveout at ANTO from eastern back-azimuths, we considered three hypotheses; (1) a dipping interface, (2) multiple reverberations in shallow layers, and (3) scattering from surface topography. A dipping Moho can advance the  $P_s$  arrival by 1 s or more, but does not induce a large negative moveout with epicentral distance, even for unrealistic dip angles ( $40^\circ$  downdip in Fig. 12). Two negative pulses on the transverse RF suffer moveout from teleseismic delays of 3.5 and 7 s to  $\sim 2.3$  and  $\sim 4.5$  s for regional RFs (Fig. 10). Hypothetically, these  $P_s$  signals could be reverberations of a  $P_s$  at 1 s delay e.g.  $P_{SSDS}$  and  $P_{S(DS)_2}$ , where  $D$  is a shallow crustal discontinuity. However, all mantle  $P$  and  $P_n$  waves approach a shallow-crustal interface at a steep incidence angle, so that moveout with epicentral distance is minimal, even for multiple reverberations (Fig. 12). Scattering from a surface heterogeneity that lies between the source and receiver can generate significant negative moveout as  $\Delta \rightarrow 0$ . Both  $P$  and  $S$  scattered waves from topography would produce receiver-function pulses, with roughly evenly-spaced delays, as long as the propagation deflections were significant. Based on this comparison, we hypothesize that the negative-moveout, negative-polarity RF pulses at ANTO from eastern backazimuths arise from a surface or near-surface scatterer some 20–30 km eastward of the station.

#### 4 MODELLING

Regional receiver functions for RAYN and for western back-azimuths, ANTO suggest that reverberative regional  $P$  waves

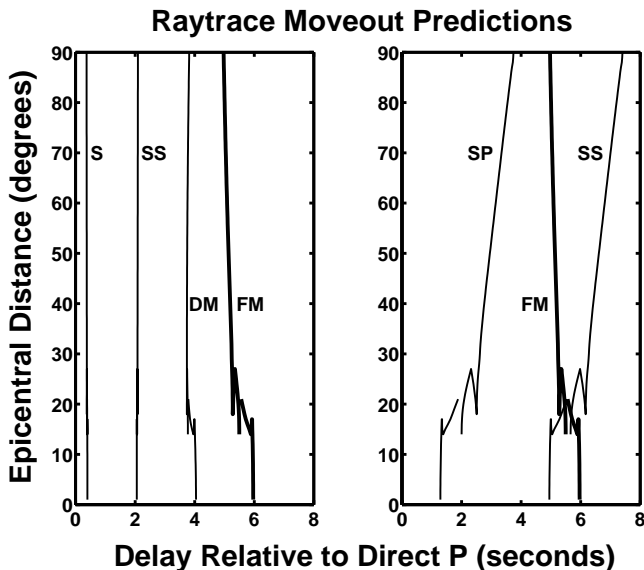


**Figure 12.** Moveout curves for simple  $P_s$  scattering scenarios, using an upgoing plane-wave approximation. Wave slowness for  $P$  and  $P_n$  phases is taken from the IASPEI91 earth model. Moho depth is 40 km beneath a hypothetical station, and crustal  $V_P$  and  $V_S$  are 6.0 and  $6/\sqrt{3}$ , respectively. The mantle  $V_P$  is  $8.0 \text{ km sec}^{-1}$ . Curve ‘FM’ indicates  $P_s$  delays for a flat Moho. Curve ‘DM’ indicates  $P_s$  delays for a Moho that dips  $40^\circ$ , with direct- $P$  approaching from the updip side. Curves ‘S’ and ‘SS’ in the left panel indicate  $P_{DS}$  and  $P_{SDS}$  phases that convert and reflect, respectively, from a shallow interface  $D$ . Curves ‘SP’ and ‘SS’ in the right panel indicate the arrivals of  $P$  and  $S$  waves, respectively, from a surface scatterer 30 km from the station, between source and receiver. Only the ‘SP’ and ‘SS’ curves have negative moveout as  $\Delta \rightarrow 0$  that resembles RF features in Fig. 10.

possess a deterministic component that constrains 1-D seismic structure in a manner analogous to a teleseismic RF. If so, it follows that features of the observed RFs should be reproducible with synthetic seismograms for 1-D velocity structures, perhaps with anisotropy. Previous studies of the regional-distance wavefield have often highlighted 3-D scattering effects (e.g. Dainty & Toksoz 1990; Wagner & Langston 1992a), so 1-D modelling might seem too simplistic. However, two factors justify wave-propagation simulations in a 1-D structure. First, the multiple-taper receiver functions are estimated only from the coherent portion of the seismic wavefield. The algorithm discards a fraction of the wavefield that is likely associated with random 3-D scatterers. Second, Wagner & Langston (1992b) and Wagner (1996) argue that array measurements of regional waves exhibit an internal coherence that is best modelled with a spatially anisotropic distribution of scatterers. For seismic wavelengths greater than the scale length of crustal velocity anomalies, a distribution of aligned high-aspect-ratio scatterers will behave (to first order) as an anisotropic medium.

We address several questions with synthetic seismograms. In a 1D medium, to what extent do  $P_g$ ,  $P_n$  or related ‘whispering gallery’ waves (Menke & Richards, 1980), exhibit delayed scattered waves that can be interpreted as  $P$ -to- $S$  conversion at the Moho? How does anisotropy in the crust and/or uppermost mantle influence the conversion? Observed radial RFs show continuity of  $P_{MS}$  across regional and teleseismic distances, but transverse RFs do not. Is this consistent with synthetic waveforms?

A significant  $P$ - $SH$  converted phase is predicted for near-horizontal-incidence direct  $P$  (Fig. 13) by the reflectivity computer code described by Levin & Park (1997b), in conflict with the weak observed signals in regional-distance transverse RFs. The conflict may arise because an incident plane wave does not capture well the extended and emergent nature of regional  $P$ , which is composed of the Moho-refracted  $P_n$  head wave and the Moho-reflected  $P_g$  phase.  $P_n$  and  $P_g$  are represented more properly by leaky modes of the crust. To compute more realistic synthetic seismograms, we adapted the computer code described by Park (1996), appropriate for surface waves in layered anisotropic media. We adopted a locked-mode approach (Harvey 1981; Gombert & Masters 1988; Cormier *et al.* 1991), rather than computing leaky modes explicitly (Haddon 1986), by bounding a flat-layered upper mantle model with a halfspace of artificially high shear velocity. Since the behaviour of waves that turn deeper in the upper mantle is, we feel, adequately modelled by our upgoing plane-wave code, we did not include the upper-mantle velocity gradient in test models. However, we placed the halfspace boundary at 660 km depth to delay the arrival of its body-wave reflections until, or beyond, the crustal surface waves.

No attempt was made to fit the observed RAYN and ANMO RFs directly, rather, we examined a collection of hypothetical models to explore their agreements and differences. All models examined possessed a midcrustal velocity jump and a modest velocity gradient just below the Moho (Fig. 14). We computed hybrid  $P$ - $S$  locked modes for  $f \leq 2$  Hz, at frequency spacing  $\Delta f = 0.001$  Hz—more than  $10^6$  modes for each model (Fig. 15). A handful of the 1000+ overtone branches were lost by the root finding algorithm, but computational experiments to retrieve the lost modes did not alter the synthetics significantly.

The synthetic  $P_n$  phase appears as a series of wavepackets that grow in amplitude, followed by  $P_g$  (Fig. 16). The  $S_n$  phase also appears as a growing series of wavepackets, followed by

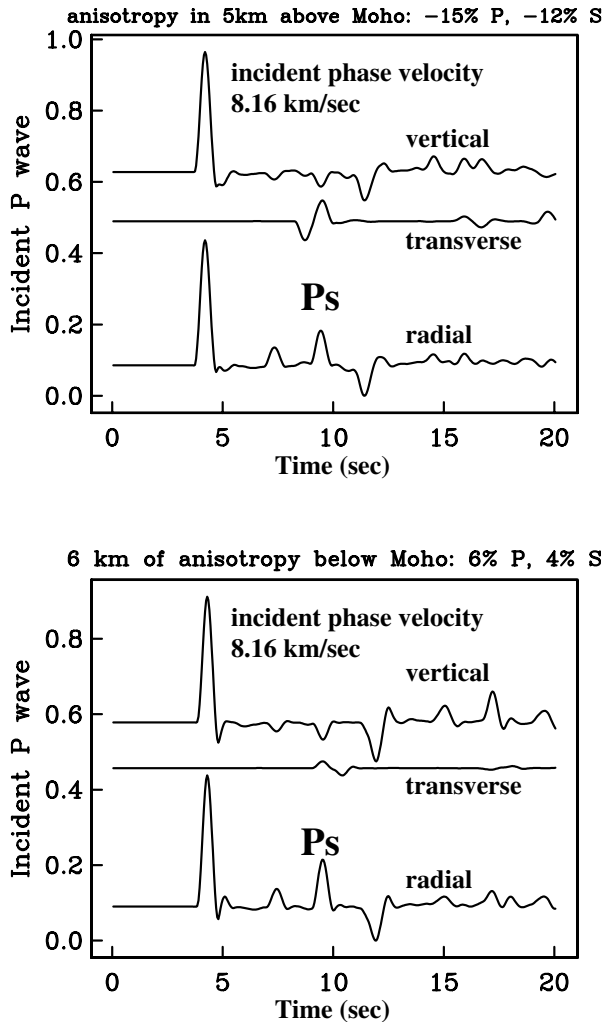


**Figure 13.** Reflectivity synthetics for upgoing compressional plane waves in two crustal structures described in the text and in Fig. 14.  $P_s$  converted phases from the Moho and from a midcrustal interface are clearly evident at roughly 5- and 3-s delay relative to direct  $P$ . Note the  $P_s$  ‘derivative’ pulses on the transverse component, generated by layers of anisotropy near the Moho. The negative pulse at  $t=11$ – $12$  s is a purely  $P$  reverberation in the upper crust. Since the ratio of component amplitudes for this reverberative phase matches that of direct  $P$ , receiver functions computed from these records would associate the phase with the zero-lag pulse at  $t=0$ .

the surface waves. Anisotropy causes coupling between  $P$ - $SV$  (Rayleigh) and  $SH$  (Love) motion, and is manifested in several ways. If the source mechanism is chosen to coincide with a Love-wave node (e.g. source azimuth  $45^\circ$  from a strike-slip fault), Love-Rayleigh coupling produces a strong Love wave where, without coupling, its amplitude would vanish. Conversely, if the source mechanism is chosen to coincide with a Rayleigh-wave node (e.g. source azimuth at  $0^\circ$  strike to a strike-slip fault), Love-Rayleigh coupling produces a strong Rayleigh wave, but little or no  $P_n$  or  $P_g$ . In many cases the  $S_n$  phase has a significant expression on the transverse component, implying distortion of  $SV$  particle motion. For the  $P_n$  and  $P_g$  phases, however, the expression on the transverse component is small, near-vanishing for  $f < 1$  Hz. Cases (1) and (4), with anisotropy concentrated near the Moho, have  $P_n$  and  $P_g$  with the smallest transverse amplitudes.

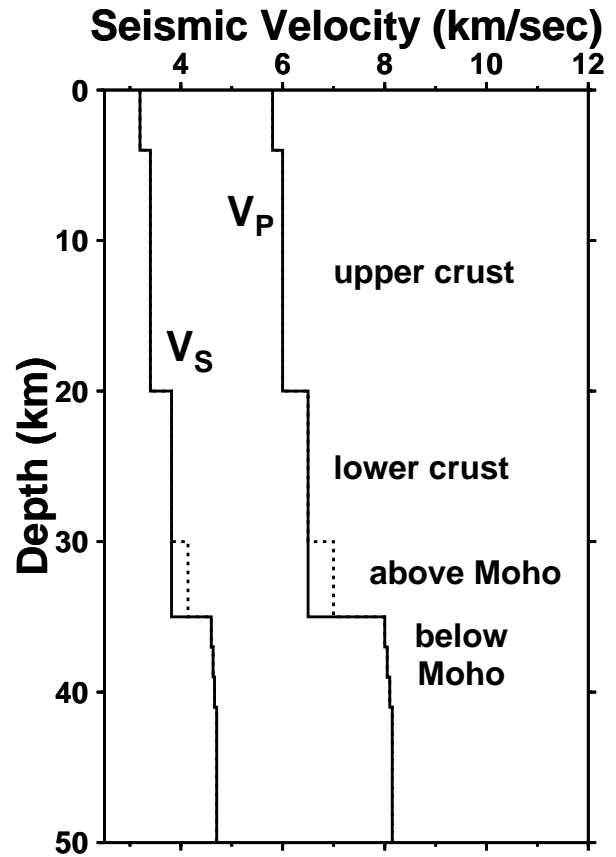


**Figure 14.** Velocity models for locked-mode reflectivity computations. We examined four arrangements of anisotropy: (1) 6%  $P$ , 4%  $S$  in the 6-km velocity gradient beneath the Moho; (2) 6%  $P$ , 4%  $S$  in a 15-km lower crustal layer; (3) 6%  $P$ , 4%  $S$  in a 16-km upper crustal layer; and (4) 15%  $P$ , 12%  $S$  in a 5-km crustal layer just above the Moho. We used an isotropic control model as a fifth case. Anisotropy similar to Case (1) is suggested by Levin & Park (2000) from teleseismic receiver function modeling at RAYN. Case (4) is based on the receiver functions at station ARU (Arti, Russia), modeled by Levin & Park (1997a) to have a slow-axis of symmetry with intermediate velocities and strong anisotropy. We specified a  $45^\circ$  dip of the anisotropy symmetry axis with horizontal strike at a  $45^\circ$  angle to the source-receiver path. This orientation converts  $P$  to  $S$  effectively (Levin & Park 1998). The dashed line indicates a basal crustal layer with velocities appropriate for a mixture of mantle and crustal rocks, used for Case (4).

To estimate receiver functions (Fig. 17), we computed discrete Fourier transforms on time intervals that included both  $P_n$  and  $P_g$ , as distinguishing the phases in real data is often problematic. We interpret a waveform at roughly 5.1 s delay as Moho-converted  $P_s$  energy. A pulse near this delay time is evident for all test models, including the isotropic control model, which suggests that the depth range of anisotropy is not a determining factor. The emergent nature of the  $P_n$  and  $P_g$  wave-trains probably accounts for acausal RF signals at negative delay times, as well as the unusual pulse shapes at zero delay. Both of these behaviours can be found in the regional  $P$  RFs observed at RAYN (Figs 6 and 7).

Our synthetic seismograms indicate that anisotropy in the lowermost crust and uppermost mantle does not easily induce  $P$ -to- $SH$  conversion at the Moho in regional  $P$  waves. Anisotropy in the crust is more efficient at boosting the transverse RF in synthetics, but often at near-zero delay i.e. largely a

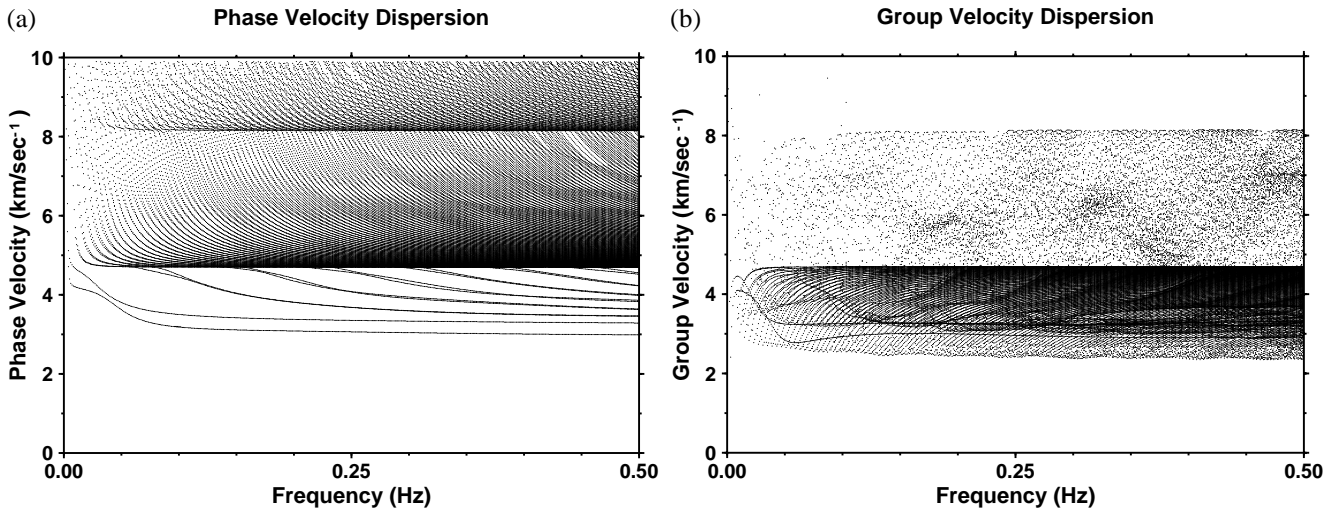


**Figure 15.** Dispersion diagrams for locked modes in crust/mantle model with dipping-axis anisotropy in the 6-km velocity gradient below the Moho. Modal solutions for  $f \leq 0.5$  Hz are shown. In the phase velocity diagram, note the concentrations of modes at the nominal head wave velocities 8.15 and 4.7 km/sec for  $P$  and  $S$ , respectively. In the group velocity diagram, note the sharp upper bound on crustal surface-wave modes at 4.7 km/sec, above which a cloud of modal group velocities corresponds to the ‘leaky’ modes that comprise  $P_g$  and  $P_n$ .

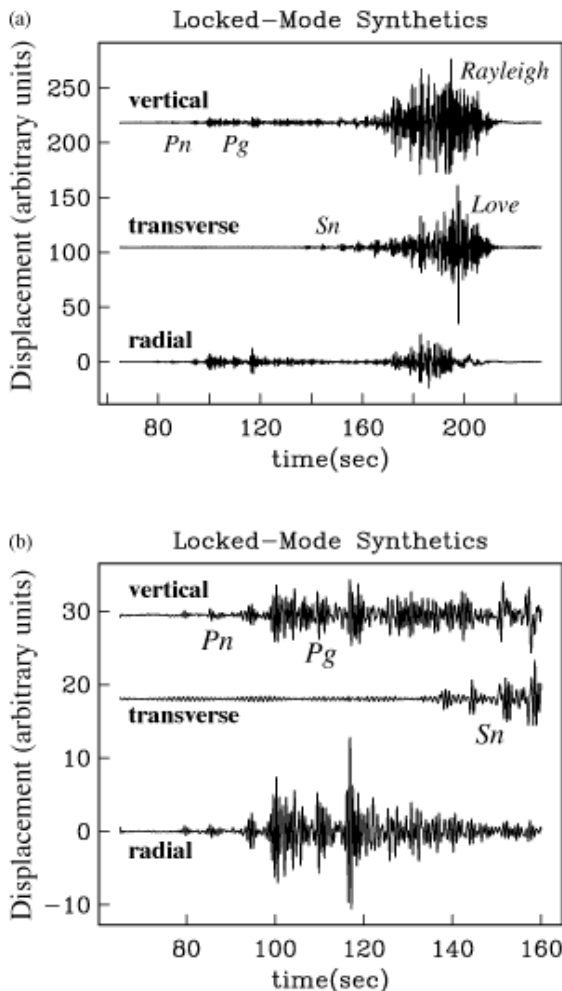


**Figure 16.** Locked-mode reflectivity synthetic seismograms of regional  $P_n$  and  $P_g$  phases. (a) Body and surface wavetrains. (b) magnifies the emergent body waves at the start of the seismogram. The model is Case (1) after the velocity profile in Fig. 14: 6%  $P$ , 4%  $S$  anisotropy in the 6-km velocity gradient below the Moho.

distortion of direct- $P$  particle motion. The synthetic RFs for 1-D structures are consistent with the observation that transverse RFs for regional  $P$  at ANTO and RAYN connect poorly with the transverse RFs for teleseismic  $P$ . For the radial component, the synthetic RFs confirm that a phase corresponding to  $P_{MS}$  can be identified, so that the continuity with teleseismic radial RFs is confirmed. The regional  $P_{MS}$  conversion is accompanied by several other  $P$ -to- $S$  conversions arising from crustal reverberations. The RFs lack a clear  $P_S$  converted phase from the midcrustal interface of the test models, suggesting that the RFs largely represent multiple reverberations in the crustal waveguide. The relative amplitudes of these secondary conversions can vary strongly with epicentral distance, consistent with the regional  $P$  receiver functions for ANTO from western back-azimuths and for RAYN (Figs 6–10).

We conclude that 2-D or 3-D structure is not required to explain the gross characteristics of the observed regional RFs. This conclusion does not exclude 3-D structure from contributing to the RFs. The prominence of  $P_{MS}$  in the data RFs, where observed, is greater than in the synthetic RFs. A larger sub-Moho velocity gradient or 3-D refraction effects could increase the  $P$  energy that bottoms in the uppermost mantle, relative to our synthetics. Rough Moho topography might also enhance  $P$ - $S$  conversion for regional waveforms.

## 5 DISCUSSION AND SUMMARY

The extended codas of regional  $P$  waves, suggestive of intense scattering, discourage their analysis with traditional receiver-function (RF) estimation algorithms. However, reflectivity seismograms using a locked mode approximation demonstrate that the extended nature of regional  $P$  can be simulated with a 1-D model, for which off-path- and back-scattering is absent. 3-D scattering is surely present in real data from regional distances, but our spectral algorithm appears to mitigate its influence on receiver-function estimation. It is likely that, in many locations, stable receiver functions (RFs) can be estimated from regional  $P$  waves. Resolution of  $P_S$  converted energy

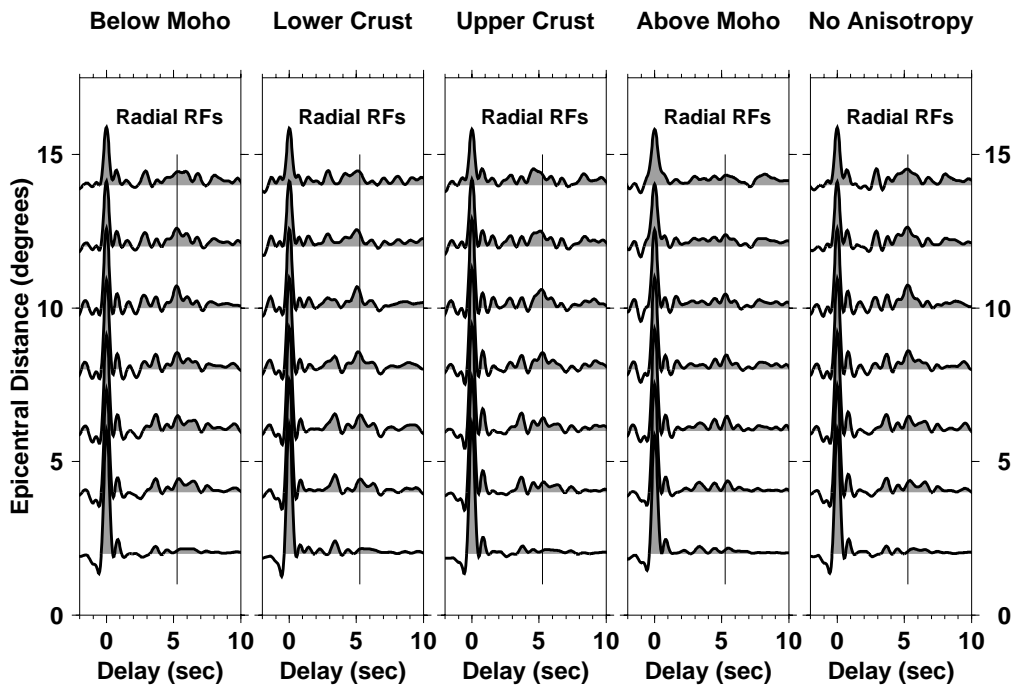


**Figure 17.** Radial receiver functions computed from locked-mode reflectivity synthetic seismograms of regional  $P_n$  and  $P_g$  phases. 42 synthetics are analyzed for each case, corresponding to epicentral distances  $X=200, 400, 600, 800, 1000, 1200$  and  $1400$  km, and an assortment of source mechanisms at different depths in the crust. Four arrangements of anisotropy were examined, as well as an isotropic control model. The thin vertical lines represent the predicted delay time of a  $P_s$  converted phase at the critical Moho incidence angle.

is greatly improved by averaging single-event RFs in the frequency domain in narrow epicentral-distance bins.

Stations RAYN and ANTO represent, to some extent, the extremes of what one might expect in receiver-function studies. RAYN lies atop a stable shield with minimal sediment cover. Primary  $P_s$  conversions from the Moho are readily retrievable at RAYN from shallow-incidence regional and near-telesismic  $P$  waves. Although sited on hard rock, ANTO lies within a river valley in an actively deforming region, close to the North Anatolian fault system. For events from the west to ANTO, Moho-converted  $P_s$  energy can be identified in the regional RFs. For events from the east to ANTO, the  $P_s$  conversions at  $f > 1$  Hz appear to be strongly influenced by shallow 3-D structures. In particular, some negative pulses in the RFs move out to shorter delays as  $\Delta \rightarrow 0$ , a behaviour we find easiest to model with  $P$ - $P$  and  $P$ - $S$  scattering from a surface or near-surface obstacle 20–30 km eastward of ANTO. For both RAYN and ANTO the radial RFs estimated from regional  $P$  agree well with the radial RFs from teleseismic  $P$ . This implies that some features in the teleseismic receiver functions for ANTO, as estimated from eastern backazimuths, may actually represent topographic scattering rather than  $P_s$  conversions from deep crustal and mantle interfaces. We conclude that receiver functions from regional  $P$  are useful to check the suitability of teleseismic receiver functions for 1-D structure inversion.

A strong east–west asymmetry in the ANTO regional- $P$  receiver functions is consistent with previous observations of regional-wave propagation. Rodgers *et al.* (1997) and Gok *et al.* (2000) report inefficient  $S_n$  and  $L_g$  propagation for regional-distance events from the east and southeast to ANTO, and efficient propagation from the west. East of ANTO lie the Turkish and Iranian plateaus, characterized by Cong & Mitchell

(1998) as having depressed shear velocities and high attenuation ( $Q < 100$  in the crust). Regional waves from the east traverse a continental collisional zone extending from central Anatolia through the Zagros mountains in southwest Iran. Broadband stations GNI (Garni, Armenia) and TBZ (Trabzon, Turkey) lie within this collision zone in eastern Anatolia. Sandvol *et al.* (1998b) and Cakir *et al.* (2000), report complex receiver functions for, respectively, GNI and TBZ, and derive models from the radial RFs with low-velocity zones in the shallow mantle. If low velocities and low  $Q$  imply subsolidus temperatures and partial melt, as suggested by Cong & Mitchell (1998) and Cakir *et al.* (2000), the propagation of regional phases would likely be disrupted.

Regional RFs for RAYN and for western backazimuths at ANTO show complexity in the inferred Moho  $P_s$  phase near  $\Delta = 20^\circ$ . This appears to be consistent with (1) the triplications of  $P$  associated with velocity gradients in the mantle transition zone, and (2) a merging of teleseismic and regional  $P$ , both of which imply overlapping phases with distinct incidence angles and (therefore) distinct  $P_s$  delay times relative to direct  $P$ . Many of the general features of regional  $P$  receiver functions are confirmed with receiver functions estimated from synthetic seismograms, computed using a locked-mode approximation with an anisotropic reflectivity code. The reverberative nature of  $P_n$  and  $P_g$  phases leads to complex radial RFs with small ‘acausal’ pulses and a train of causal pulses whose amplitude varies strongly with epicentral distance and with the details of crustal structure, all in the absence of lateral structure. Although a simple reflectivity code with an upgoing plane-wave predicts significant  $P$ -to- $SH$  conversion at the Moho at near-horizontal incidence, locked-mode synthetics suggest that regional- $P$ -to- $SH$  conversion is very weak for modest levels of anisotropy.

In the context of 1-D models, it appears possible to generate non-negligible transverse motion in regional  $P$  with anisotropy in the shallow and middle crust. However,  $P$ -to- $SH$  conversion is not as large in our synthetics as would appear to be the case in regional RFs from RAYN and ANTO. Either shallow crustal anisotropy is much larger than  $\sim 5\%$  or scattering from 2-D and 3-D structures is pervasive in the observed phases.

## ACKNOWLEDGMENTS

This work has been supported by Defense Threat Reduction Agency Contract DSWA01-98-011. We thank W. Menke for suggesting the importance of travel-time triplications. Gary Pavlis provided a perceptive review. We used GMT software (Wessel & Smith 1991) to prepare figures. Seismic data were obtained from the IRIS Data Management System archive.

## REFERENCES

- Abers, G.A., Hu, X. & Sykes, L.R., 1995. Source scaling of earthquakes in the Shumagin region, Alaska: time-domain inversions of regional waveforms, *Geophys. J. Int.*, **123**, 41–58.
- Al-Amri, A., 1999. The crustal and upper-mantle structure of the interior Arabian Platform, *Geophys. J. Int.*, **136**, 421–430.
- Ammon, C.J., 1991. The isolation of receiver effects from teleseismic  $P$  waveforms, *Bull. seism. Soc. Am.*, **81**, 2504–2510.
- Badri, M., 1991. Crustal structure of central Saudi Arabia from seismic refraction profiling, *Tectonophysics*, **185**, 357–374.
- Burdick, L.J. & Langston, C.A., 1977. Modeling crustal structure through the use of converted phases in teleseismic body-wave forms, *Bull. seism. Soc. Am.*, **67**, 677–691.
- Cakir, O., Erduran, M., Cinar, H. & Yilmazturk, A., 2000. Forward Modelling receiver functions for crustal structure beneath station TBZ (Trabzon, Turkey), *Geophys. J. Int.*, **140**, 341–356.
- Cong, L. & Mitchell, B.J., 1998. Seismic velocity and  $Q$  structure of the Middle Eastern crust and upper mantle from surface wave dispersion and attenuation, *Pure appl. Geophys.*, **153**, 503–538.
- Cormier, V.F., Mandal, B. & Harvey, D., 1991. Incorporation of velocity gradients in the synthesis of complete seismograms by the locked mode method, *Bull. seism. Soc. Am.*, **81**, 897–930.
- Dainty, A.M., & Toksoz, M.N., 1990. Array analysis of seismic scattering, *Bull. seism. Soc. Am.*, **80**, 2242–2260.
- Gok, R., Turkelli, N., Sandvol, E., Seber, D. & Barazangi, M., 2000. Regional wave propagation in Turkey and surrounding regions, *Geophys. Res. Lett.*, **27**, 429–432.
- Gomberg, J.S. & Masters, T.G., 1988. Waveform modeling using locked mode synthetic and differential seismograms: Application to determination of the structure of Mexico, *Geophys. J.*, **94**, 193–218.
- Gurrola, H., Baker, F.G. & Minster, J.B., 1995. Simultaneous time-domain deconvolution with application to the computer of receiver functions, *Geophys. J. Int.*, **120**, 537–543.
- Haddon, R.A.W., 1986. Exact evaluation of the response of a layered elastic medium to an explosive point source using leaking modes, *Bull. seism. Soc. Am.*, **76**, 1755–1775.
- Hales, A.L., 1969. A seismic discontinuity in the lithosphere, *Earth planet. Sci. Lett.*, **7**, 44–46.
- Hales, A.L., Muirhead, K.J., Rynn, J.M. & Gettrust, J.F., 1975. Upper-mantle travel times in Australia—A preliminary report, *Phys. Earth planet. Inter.*, **11**, 109–118.
- Harvey, D., 1981. Seismogram synthesis using normal mode superposition: The locked mode method, *Geophys. J. R. astr. Soc.*, **66**, 37–61.
- Kahle, H.-G., Cocard, M., Peter, Y., Geiger, A., Reilinger, R., McClusky, S., King, R., Barka, A. & Veis, G., 1999. The GPS strain rate field in the Aegean Sea and western Anatolia, *Geophys. Res. Lett.*, **26**, 2513–2516.
- Langston, C.A., 1981. Evidence for the subducting lithosphere under southern Vancouver Island and western Oregon from teleseismic  $P$  wave conversions, *J. geophys. Res.*, **86**, 3857–3866.
- Lees, J., Park, J., 1995. Multiple-taper spectral analysis: A stand-alone C-subroutine, *Computers Geosci.*, **21**, 199–236.
- Levin, V. & Park, J., 1997a. Crustal anisotropy beneath the Ural mountains foredeep from teleseismic receiver functions, *Geophys. Res. Lett.*, **24**, 1283–1286.
- Levin, V. & Park, J., 1997b.  $P$ - $SH$  conversions in a flat-layered medium with anisotropy of arbitrary orientation, *Geophys. J. Int.*, **131**, 253–266.
- Levin, V. & Park, J., 1998. A  $P$ - $SH$  conversion in layered media with hexagonally symmetric anisotropy: A cookbook, *Pure appl. Geophys.*, **151**, 669–697.
- Levin, V. & Park, J., 2000. Shear zones in the Proterozoic lithosphere of the Arabian Shield and the nature of the Hales discontinuity, *Tectonophysics*, **323**, 131–148.
- Menke, W., Lerner-Lam, A., Dubendorff, B. & Pacheco, J., 1990. Polarization and coherence of 5–30 Hz seismic wavefields at a hard rock site and their relevance to velocity heterogeneities in the crust, *Bull. seism. Soc. Am.*, **80**, 430–449.
- Menke, W., Richards, P.G., 1980. Crust-mantle whispering-gallery phases: A deterministic model of  $P_n$  wave propagation, *J. geophys. Res.*, **85**, 5416–5422.
- Mooney, W.D., Gettings, M.E., Blank, H.R. & Healy, J., 1985. Saudi Arabian deep refraction profile, *Tectonophysics*, **111**, 173–246.
- Park, J., 1996. Surface waves in layered anisotropic structures, *Geophys. J. Int.*, **126**, 173–184.
- Park, J., Lindberg, C.R. & Vernon, F.L., 1987. Multitaper spectral analysis of high-frequency seismograms, *J. geophys. Res.*, **92**, 12 675–12 684.
- Park, J. & Levin, V., 2000. Receiver functions from multiple-taper spectral correlation estimates, *Bull. seism. Soc. Am.*, **90**, 1507–1520.
- Prodehl, C., 1985. Interpretation of a seismic refraction survey across the Arabian Shield in western Saudi Arabia, *Tectonophysics*, **111**, 247–282.
- Rodgers, A.J., Ni, J.F. & Hearn, T.M., 1997. Propagation characteristics of short-period  $S_n$  and  $L_g$  in the Middle East, *Bull. seism. Soc. Am.*, **87**, 396–413.
- Sandvol, E., Seber, D., Barazangi, M., Vernon, F.L., Mellors, R. & Al-Amri, A., 1998a. Lithospheric seismic velocity discontinuities beneath the Arabian Shield, *Geophys. Res. Lett.*, **25**, 2873–2876.
- Sandvol, E., Seber, D., Calvert, A. & Barazangi, M., 1998b. Grid search modelling of receiver functions; implications for crustal structure in the Middle East and North Africa, *J. geophys. Res.*, **103**, 26 899–26 917.
- Thomson, D.J., 1982. Spectrum estimation and harmonic analysis, *IEEE Proc.*, **70**, 1055–1096.
- Wagner, G.S., 1996. Numerical simulations of wave propagation in heterogeneous wave guides with implications for regional wave propagation and the nature of lithospheric heterogeneity, *Bull. seism. Soc. Am.*, **86**, 1200–1206.
- Wagner, G.S., Langston, C.A., 1992a. Body-to-surface wave scattered energy in teleseismic coda observed at the NORESS seismic array, *Bull. seism. Soc. Am.*, **82**, 2126–2138.
- Wagner, G.S., Langston, C.A., 1992b. A numerical investigation of scattering effects for teleseismic plane wave propagation in a heterogeneous layer over a homogenous halfspace, *Geophys. J. Int.*, **110**, 486–500.
- Wessel, P. & Smith, W.H.F., 1991. Free software helps map and display data, *Eos, Trans. Am. geophys. Un.*, **72**, 441.